

In vivo imaging of brain glutamate defects in a knock-in mouse model of Huntington's disease



Jérémy Pépin^{a,b}, Laetitia Francelle^{a,b}, Maria-Angeles Carrillo-de Sauvage^{a,b}, Lucie de Longprez^{a,b}, Pauline Gipchtein^{a,b}, Karine Cambon^{a,b}, Julien Valette^{a,b}, Emmanuel Brouillet^{a,b}, Julien Flament^{a,c,*}

^a Commissariat à l'Energie Atomique (CEA), Direction de la Recherche Fondamentale (DRF), Institut d'Imagerie Biomédicale (I2BM), Molecular Imaging Research Center (MIRcen), F-92260 Fontenay-aux-Roses, France

^b Centre National de la Recherche Scientifique (CNRS), Université Paris-Sud, Université Paris-Saclay, UMR 9199, Neurodegenerative Diseases Laboratory, F-92260 Fontenay-aux-Roses, France

^c Institut national de la santé et de la recherche médicale (Inserm), UMS 27, F-92260 Fontenay-aux-Roses, France

ARTICLE INFO

Article history:

Received 3 February 2016

Revised 10 June 2016

Accepted 14 June 2016

Available online 16 June 2016

Keywords:

Chemical exchange saturation transfer

GluCEST

Huntington's disease

Glutamate

Mouse model

Neurodegenerative disease

ABSTRACT

Huntington's disease (HD) is an inherited neurodegenerative disease characterized by motor, cognitive and psychiatric symptoms. Atrophy of the striatum has been proposed for several years as a biomarker to assess disease progression in HD gene carriers. However, it does not provide any information about the biological mechanisms linked to HD pathogenesis. Changes in brain metabolites have been also consistently seen in HD patients and animal models using Magnetic Resonance Spectroscopy (MRS), but metabolite measurements are generally limited to a single voxel. In this study, we used Chemical Exchange Saturation Transfer imaging of glutamate (gluCEST) in order to map glutamate distribution in the brain of a knock-in mouse model (Ki140CAG) with a precise anatomical resolution. We demonstrated that both heterozygous and homozygous mice with pathological CAG repeat expansion in gene encoding huntingtin exhibited an atrophy of the striatum and a significant alteration of their metabolic profile in the striatum as compared to wild type littermate controls. The striatal decrease was then confirmed by gluCEST imaging. Surprisingly, CEST imaging also revealed that the corpus callosum was the most affected structure in both genotype groups, suggesting that this structure could be highly vulnerable in HD. We evaluated for the first time gluCEST imaging as a potential biomarker of HD and demonstrated its potential for characterizing metabolic defects in neurodegenerative diseases in specific regions.

© 2016 The Authors. Published by Elsevier Inc. This is an open access article under the CC BY-NC-ND license (<http://creativecommons.org/licenses/by-nc-nd/4.0/>).

Introduction

Huntington's disease (HD) is an inherited neurodegenerative disorder characterized by involuntary abnormal movements, as well as cognitive and psychiatric symptoms associated with early atrophy of the striatum and cerebral cortex (Harper, 1991; Walker, 2007). The mutation causing HD consists of an abnormal expansion of a CAG repeat in the gene coding the protein huntingtin (htt). There is no therapy to slow the progression of the disease which is fatal in 10–15 years after the onset of symptoms in young individuals. Despite active research in the past twenty years, the mechanisms underlying brain dysfunction and degeneration remain poorly understood. Mutation of huntingtin affects many cellular processes such as transcription (Sugars and Rubinsztein, 2003), neurotransmission, calcium homeostasis (Cowan and Raymond, 2006), autophagy and energy metabolism (Bossy et al.,

2008; Damiano et al., 2010; Mochel et al., 2007; Mochel and Haller, 2011) in both neurons and astrocytes.

There is a limited number of methods allowing precise follow up of disease progression and understanding of physiopathological pathways. Clinical assessments along with neuroimaging techniques are likely the most robust criteria to characterize disease severity in HD patients. For instance, the atrophy of the striatum as measured by MRI is currently the best biomarker of disease progression in HD gene carriers (Aylward et al., 2004; Paulsen et al., 2008; Tabrizi et al., 2013). However, although anatomical alterations seen by MRI can be found many years before onset of symptoms in HD gene carriers, they do not provide any information about the biological mechanisms linked to HD pathogenesis. In the case of clinical trials, morphometric MRI might be crucial to determine whether the therapy modifies or slows down atrophy but does not give rapid indication about biological efficacy of the treatment. Thus, there is a need to develop novel “functional” imaging modalities. Defects in brain energy metabolism have been consistently found in HD patients and animal models. In particular, Positron Emission Tomography (PET) studies demonstrated large reduction in glucose consumption in the caudate/putamen in HD patients (Brouillet et al.,

* Corresponding author at: MIRcen, 18 route du Panorama – BP n° 6, 92265 Fontenay-aux-Roses Cedex, France.

E-mail address: julien.flament@cea.fr (J. Flament).

1999; Kuwert et al., 1989, 1990). Nonetheless, non-invasive *in vivo* methods to more broadly characterize energy metabolism in HD are rare. *In vivo* Magnetic Resonance Spectroscopy (MRS) can provide key insights of pathological molecular processes related to cell metabolism. Analysis of human HD cohorts or transgenic mouse models of HD using *in vivo* ^1H or ^{31}P MRS methods suggested early metabolic changes in the brain (Jenkins et al., 1998; Mochel et al., 2012; Sturrock et al., 2010; Zacharoff et al., 2012). Interestingly, several studies using ^1H MRS showed that the concentrations of glutamate and *N*-acetyl-aspartate, two metabolites mainly located in neurons, were decreased in HD patients and animal models (Jenkins et al., 1998, 2000, 2005). Glutamate is the major excitatory transmitter in the central nervous system and is involved in several aspects of normal brain functions including cognition, memory and learning. Its concentration in the brain is higher than all other amino acids (around 10 mmol/kg), and it plays a central role in brain metabolism (Sonnewald, 2014). Regulatory system of glutamate concentration in the brain is very complex (Magistretti and Allaman, 2015). In normal conditions, most of glutamate is located in cells, neurotransmission being governed by few micromolar of extracellular glutamate. Glutamate can become toxic if extracellular concentration is too high. In such case, glutamate overactivates ionotropic glutamate receptors, and producing major rise in Ca^{2+} concentration in the cytoplasm of neurons, triggers excitotoxicity (Beal, 2005; Brouillet et al., 1999; Cowan and Raymond, 2006). Thus, mechanisms to maintain low extracellular concentration are crucial for brain functions. In addition to its major role as an excitatory neurotransmitter, glutamate is central to several metabolic pathways related to energy metabolism and oxidative stress. For instance, it is involved in many crucial biological pathways such as the tricarboxylic acid (TCA) cycle (it is in exchange with TCA cycle intermediate α -ketoglutarate), regulation of glutathione synthesis and astrocyte–neuron interactions. Consequently, glutamate concentration has to be precisely regulated and a small defect can be very deleterious for the brain.

In this context, ^1H MRS has been widely used to precisely monitor alterations of metabolic profiles and particularly glutamate concentration. However, one important limitation of MRS is that glutamate measurements are confined to relatively large voxels, due to limited sensitivity of the method. Thus, it would be of major interest to find functional biomarkers related to energy metabolism that could be monitored in the entire brain and with good anatomical resolution in HD animal models or gene carriers. Recently, CEST (Chemical Exchange Saturation Transfer) has been proposed to indirectly detect dilute molecules with labile protons (Ward et al., 2000; Ward and Balaban, 2000; Wolff and Balaban, 1990). Exchangeable protons, for example amine ($-\text{NH}_2$) or amide ($-\text{NH}$) groups, exhibit a resonance frequency that is shifted relative to bulk proton frequency. Likewise, exchangeable protons can be selectively saturated using radiofrequency (RF) pulse, leading to a decrease of water signal due to magnetization exchange. The potential of CEST imaging to map glutamate level has already been demonstrated in both rodent and human brains at high magnetic fields (≥ 7 T) (Cai et al., 2012, 2013; Carrillo-de Sauvage et al., 2015). It is thus possible to map local alteration in glutamate concentrations, which may be a potential indicator of regional energy defects *in vivo*.

Here, we investigated whether gluCEST could represent a relevant biomarker of HD. To do so, we studied a knock-in (Ki) mouse model of HD. Several Ki mouse models have already been described in the literature expressing various length of CAG triplet, from 50 to 175 (Lin et al., 2001; Menalled, 2005; Wheeler et al., 2002). These Ki mice are usually characterized by the slowly progressive appearance of the symptoms, which mimics more closely human HD pathology than severe and rapid mouse models (Lin et al., 2001; Menalled and Chesselet, 2002; Menalled et al., 2003; Wheeler et al., 2000). In the present study, we developed and applied gluCEST imaging to examine brain glutamate concentrations in a slowly progressing mouse model of HD, the Ki mice expressing chimeric mouse/human exon 1 containing

140 CAG repeats inserted in the murine Htt gene (Ki140CAG) (Menalled et al., 2003).

Materials and methods

Ki140CAG and wild type littermate mice

Mice were housed in a temperature-controlled room maintained on a 12 h light/dark cycle. Food and water were available *ad libitum*. All animal studies were conducted according to the French regulation (EU Directive 2010/63/EU – French Act Rural Code R 214-87 to 131). The animal facility was approved by veterinarian inspectors (authorization n° A 92-032-02) and complies with Standards for Humane Care and Use of Laboratory Animals of the Office of Laboratory Animal Welfare (OLAW – n° #A5826-01). All procedures received approval from the ethical committee (authorization n°2015060417243726vl (APAFIS#770).

In the present study, we used knock-in mice expressing chimeric mouse/human exon 1 containing 140 CAG repeats inserted in the murine Htt gene (Ki140CAG). Ki140CAG mice colony was maintained by breeding heterozygotes Ki140CAG males and females (Menalled et al., 2003). Mice were N3 (B6) on a 129 Sv \times C57BL/6J background. Genotype was determined from PCR of tail snips taken at 10–15 days of age for Ki140CAG mice. The resulting mice of our colony were divided in 2 groups depending on their genotype; heterozygous and homozygous for the Htt gene. Ki140CAG mice were compared to their wild type (WT) littermate controls.

Preliminary behavioral testing of the Ki140CAG mouse colony

Open-field test

We used groups of WT ($n = 3$, 3 females), heterozygous ($n = 5$, 3 females, 2 males), and homozygous ($n = 8$, 5 females, 3 males) mice. The three groups of 7–15 month-old mice were matched for age (mean \pm SEM in months: WT, 9.33 ± 1.86 ; heterozygous, 11.10 ± 2.68 ; homozygous, 11.81 ± 0.72) and were not statistically different in body weight (mean \pm SEM in grams: WT, 27.30 ± 0.51 ; heterozygous, 29.05 ± 2.9 ; homozygous 26.47 ± 1.21). We assessed the spontaneous locomotor activity of Ki140CAG mice in an automated Ethovision XT/open-field apparatus (Noldus). Mice were transferred to the testing room and allowed to acclimate for at least 30 min before testing. The open-field consisted of a square arena (50×50 cm, 40 cm high). The floor was divided into two virtual concentric parts, with an inner zone in the middle of the arena (25×25 cm) and an outer zone extending from the outer edge of the inner zone to the walls of the structure. Animals were placed in the center of the arena at the start of the test. Locomotor activity was monitored for 10 min with a video camera mounted on the ceiling directly above the center of the arena. The floor of the arena was washed with 70% ethanol between tests, to remove the odor of the previous subject. A computerized tracking system (Ethovision XT, Noldus IT) calculated total locomotion, speed, and time spent immobile by image analysis. We also recorded duration of rearing and grooming behavior during the 10 min trial by visual inspection of the behavior of each animal using time encoded video recording (the Observer, Noldus).

Rotarod test

We used groups of WT ($n = 5$, 4 females, 1 male), heterozygous ($n = 9$, 1 female, 8 males), and homozygous ($n = 10$, 4 females, 6 males) mice. Mice were different from those used for the open-field test. The three groups of 10–13 month-old mice were matched for age (mean \pm SEM in months: WT, 10.60 ± 1.03 ; heterozygous, 11.10 ± 0.33 ; homozygous, 11.50 ± 0.52) and were not statistically different in body weight (mean \pm SEM in grams: WT, 28.22 ± 0.79 ; heterozygous, 28.03 ± 0.74 ; homozygous 26.27 ± 0.83). The rotarod test was used to evaluate the motor coordination and strength of the mice.

Mice were trained on a rotarod (MED-Associates Rota-Rod) at 4 rotations per minute (rpm) for 5 min. They were then tested in three consecutive trials, each lasting 5 min, in which the speed of the rod was increased from 4 to 40 rpm. Mice were allowed to recover for 45 min between trials. The latency to fall (in second) in the three trials was recorded for each mouse. Values were averaged across all trials. This sequence was repeated on three consecutive days.

Immunohistochemistry

Mice received a lethal dose of sodium pentobarbital solution (50 µg per gram body weight, intraperitoneal). The brain of the animals were removed, left-hemisphere was post-fixed overnight in 4% PFA in phosphate buffer (PB) solution, then cryoprotected by immersion in 30% sucrose for 36 h. Free-floating 30-µm serial coronal sections throughout the striatum were collected serially (interspace, 240 µm), with a freezing sliding microtome (SM2400; Leica Microsystems, Wetzlar, Germany). Brain slices were placed in a storage solution (30% glycerol, 30% ethylene glycol in 0.1 M PB) and stored at -20°C before use. Brain slices were pretreated in 0.3% H_2O_2 , blocked in 4.5% NGS (Sigma), and incubated for 48 h at 4°C with primary antibodies directed against NeuN (1:2000, mouse; Millipore) or EM48 (1:200, mouse; Millipore). After rinsing, brain slices were incubated with biotinylated secondary anti-mouse antibody (1:1000; Vector Laboratories) for 1 h at room temperature. Finally, they were incubated with the Vectastain Elite ABC Kit (Vector Laboratories) and revealed with the DAB kit (Vector Laboratories).

Anatomical MRI and proton magnetic resonance spectroscopy (^1H MRS)

High resolution MRI and ^1H MRS experiments were performed on a horizontal 11.7 T Bruker scanner (Bruker, Ettlinger, Germany). We used groups of 12-month-old WT ($n = 5$, 5 males), heterozygous ($n = 5$, 4 females, 1 male), and homozygous ($n = 5$, 4 females, 1 male) mice. Mice were different from those used for behavioral tests. Mice were anesthetized using 3% isoflurane in a 1:1 gas mixture of air/ O_2 and positioned in a dedicated stereotaxic frame with mouth and ear bars to prevent any movements during MR acquisitions. Mice temperature was monitored with an endorectal probe and maintained at 37°C with regulated water flow and respiratory rate was continuously monitored using PC SAM software (Small Animal Instruments, Inc., Stony Brook, NY, USA) during scanning. The isoflurane level was adjusted around 1.5% to keep the respiratory rate in the range of 60 to 80 per minute. A quadrature cryoprobe (Bruker, Ettlinger, Germany) was used for radiofrequency transmission and reception. High resolution anatomical T_2 -weighted images acquired with Multi Slices Multi Echoes (MSME) sequence (TE/TR = 5/2500 ms, 17 echoes, effective TE = 45 ms, in-plane resolution = $70 \times 70 \mu\text{m}^2$, 25 slices with thickness = 300 µm) in coronal orientation were used for accurate delineation of structures. The same high resolution images were used to accurately position a voxel of $2 \times 2 \times 2 \text{ mm}^3$ in the left striatum. The homogeneity of the magnetic field was performed using Bruker MAPSHIM routine and good shimming was reached in the voxel (between 10.5 and 15 Hz). ^1H MRS acquisitions were performed using a LASER (Localization by Adiabatic Selective Refocusing) sequence (echo time (TE)/repetition time (TR) = 20/5000 ms combined with VAPOR water suppression. Metabolites spectra were acquired using 128 repetitions for a total scan time of 10 min. Metabolite concentrations were quantified using LCModel (Provencher, 1993) and the macromolecule (MM) spectrum of a control mouse was determined by metabolite nulling and included in the base set for LCModel. The following metabolites were reliably quantified (Cramér-Rao lower bound (CRLB) < 5% in all experiments): total choline (total glycerophosphocholine + phosphocholine + choline, tCho), total creatine (creatine + phosphocreatine, tCr), glutamate (Glu), glutamine (Gln), myo-inositol (Ins), total *N*-acetyl-aspartate + *N*-acetyl-aspartyl-glutamate

(NAA + NAAG, tNAA) and taurine (Tau). Metabolite concentrations were normalized with respect to 8 mM tCr.

Chemical Exchange Saturation Transfer imaging of glutamate (gluCEST)

GluCEST was performed on the same magnet with a volume coil for radiofrequency transmission and a quadrature surface coil for reception (Bruker, Ettlinger, Germany). Three gluCEST images centered on the mid-striatum were acquired with a 2D fast spin-echo sequence preceded by a frequency-selective continuous wave saturation pulse ($150 \times 150 \mu\text{m}^2$ in-plane resolution, 0.6 mm slice thickness, echo time = 6 ms, repetition time = 5000 ms, 10 echoes and effective echo time = 30 ms). The MAPSHIM routine was applied in a voxel encompassing the slices of interest in order to reach a good shim on gluCEST images. GluCEST images were acquired with a saturation pulse applied during $T_{\text{sat}} = 1$ s, composed by 10 broad pulse of 100 ms, with 20 µs inter-delay and an amplitude $B_1 = 5 \mu\text{T}$. The frequency of the saturation pulse $\Delta\omega$ was applied in a range from -5 ppm to 5 ppm with a step of 0.5 ppm. A set of CEST images was also acquired with a weak saturation amplitude ($B_1 = 0.2 \mu\text{T}$) around the water frequency ($\Delta\omega$ in a range from -1 ppm to 1 ppm with a step of 0.1 ppm) in order to correct for B_0 inhomogeneities using the Water Saturation Shift Reference (WASSR) method (Kim et al., 2009). Before gluCEST protocol, a B_1 map was acquired with the double angle method (Stollberger and Wach, 1996). Two images with long repetition time (TR = 15.000 ms) were acquired with preparation pulses flip angles of either 30° or 60° . The same normalization method, using RF pulse amplitude for a flip angle of 30° ($B_{1\text{ref}}$), as proposed in the literature was used to calculate relative B_1 map ($B_1/B_{1\text{ref}}$, unitless) (Cai et al., 2012). In vivo, CEST contrast can be hampered by several competing factors such as direct saturation transfer (DS) of free water and background magnetization transfer (MT). Although DS is symmetrical with respect to water frequency and its contribution to CEST contrast can be suppressed by asymmetrical analysis (van Zijl and Yadav, 2011; Zhou and van Zijl, 2006), it is not always the case for MT background. However, it has been shown that MT asymmetry was minimized with high saturation amplitude (Sun et al., 2005), which is the case for gluCEST imaging ($B_1 = 5 \mu\text{T}$).

Data processing and statistical analyses

All image processing and analyses were performed using in-house programs developed on MATLAB software (MathWorks Inc., Natick, MA). Striatum was manually delineated slice-by-slice by a single operator using high resolution images and volume was calculated for each animal.

CEST images were processed pixel-by-pixel and analyzed using in-house programs developed on MATLAB software used to generate Z-spectra by plotting the longitudinal magnetization as a function of saturation frequency. WASSR method was used to generate absolute B_0 map by finding the actual frequency within each voxel. Z-spectrum in each voxel was interpolated using a cubic spline and B_0 map was used to correct for B_0 inhomogeneities. The specific glutamate contribution was isolated using Asymmetrical Magnetization Transfer Ratio (MTRasym) (Liu et al., 2010) and was calculated as follows: $\text{MTRasym}(\Delta\omega) = 100 \times (M_{\text{sat}}(-\Delta\omega) - M_{\text{sat}}(+\Delta\omega)) / M_{\text{sat}}(-5 \text{ ppm})$, $M_{\text{sat}}(\pm\Delta\omega)$ being the magnetization acquired with saturation pulse applied at '+' or '-' $\Delta\omega$ ppm. GluCEST images were calculated with $\Delta\omega$ centered at ± 3 ppm. In order to perform regional analysis of gluCEST contrast, several Regions of Interest (ROIs) were manually drawn with help of the Allen mouse brain atlas. Segmentation was performed slice-by-slice by a single operator using the reference CEST image acquired without saturation. Variation of gluCEST contrast between WT littermates vs. heterozygous mice or between WT littermates vs. homozygous mice was calculated in each ROI as

follows: $\text{Variation} = 100 \times (\text{MTRasym}(\text{WT}) - \text{MTRasym}(\text{Ki140CAG})) / \text{MTRasym}(\text{WT})$.

Statistical analyses were performed using Statistica (StatSoft, Inc., Tulsa, OK, USA) software. Mean and standard error of the mean of all measures are reported in mean \pm SEM format throughout. The Shapiro–Wilk test was used to test the data for normality and no deviation from normality was observed for any data. One-way ANOVA (factorial) was used to compare mean values (striatal volume, metabolite ratios measured by ^1H MRS, gluCEST contrast and open-field data) of each genotype groups. For the analysis of the rotarod data, one-way ANOVA with repeated measures (days 1, 2 and 3) was used. The significant threshold was set to 0.05. ANOVA was followed by a Fisher's Least Significant Difference (LSD) post-hoc test to determine individual significant differences between groups.

Results

Behavioral tests and histology

In the rotarod test, both heterozygous and homozygous mice showed significantly poorer performance than WT littermates (Fig. 1.a, green and red lines respectively). Homozygous and heterozygous mice appeared similarly affected when comparing the latency to fall (approximately 35% reduction) with that of WT littermates (heterozygous, $p < 0.0001$; homozygous, $p < 0.006$).

In the open-field, locomotor behavior was characterized by the duration of the rearing behavior, the duration of grooming behavior and the total distance travelled during the trials (Fig. 1.b, c and d respectively). Both heterozygous and homozygous mice showed poorer

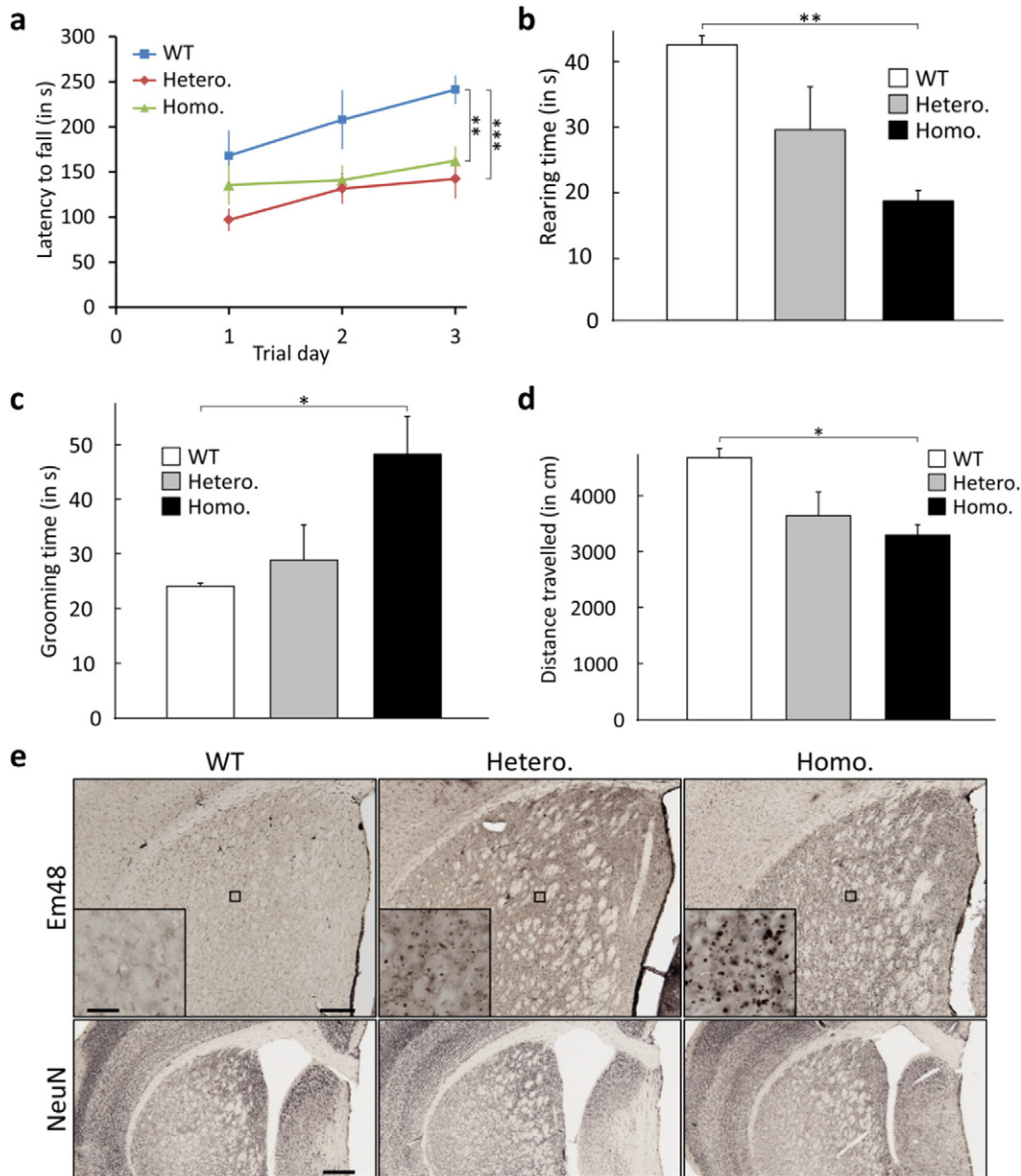


Fig. 1. Behavioral and histological characterization of Ki140CAG mouse colony. a) Rotarod test was used to evaluate the motor coordination and strength of WT littermate controls, heterozygous and homozygous mice (blue, green and red curves respectively, mean \pm SEM, $n = 5, 9$ and 10 respectively). Statistical analysis was performed by one-way ANOVA (repeated measures over days 1, 2 and 3, significant threshold set to 0.05) with Fisher's LSD post-hoc test ($***p < 0.001$; $**p < 0.01$; $*p < 0.05$). b–d) Open-field test was used to evaluate locomotor activity of WT littermate controls, heterozygous and homozygous mice (white, gray and black bars respectively, mean \pm SEM, $n = 3, 5$ and 8 respectively): rearing time (b), grooming time (c) and distanced travelled (d). Statistical analysis was performed by one-way ANOVA (factorial analysis, significant threshold set to 0.05) with Fisher's LSD post-hoc test ($***p < 0.001$; $**p < 0.01$; $*p < 0.05$). e) Representative images of immunostaining for EM48 (mutant huntingtin-containing inclusions, zoom in the black box, top panel) and NeuN (neurons, bottom panel). Scale bar: small panels = $20 \mu\text{m}$; large panels = $250 \mu\text{m}$ for Em48 and $400 \mu\text{m}$ for NeuN images.

performance as compared to WT littermates: the rearing behavior and the total distance moved were reduced (Fig. 1.b and d respectively) while grooming behavior was increased (Fig. 1.c). Statistical analysis showed that homozygous mice were significantly different from WT littermates (rearing duration, $p < 0.003$; grooming duration, $p < 0.05$; distance moved, $p < 0.02$) while there was only a trend in heterozygous mice.

We also checked that the Ki140CAG mice of our colony had huntingtin-containing aggregates, a hallmark of the pathology in HD patients. Consistent with pioneering observations (Menalled et al., 2003), we observed numerous mutant huntingtin-containing inclusions in striatum and cerebral cortex of adult Ki140CAG mice. Qualitatively, homozygous mice displayed a much higher density of inclusions as compared to heterozygous mice (Fig. 1.e, top panel). Qualitative analysis of sections stained for NeuN immunohistochemistry, a neuronal marker, neither indicated major neuronal loss nor major striatal atrophy in Ki140CAG mice when compared to WT littermates (Fig. 1.e, bottom panel).

Striatal volume by MRI

Previous studies have already demonstrated that brain atrophy can occur several years before disease onset in HD gene carriers or early in rodent HD models (Boussicault et al., 2014; Lerch et al., 2008; Rocher et al., 2016; Sawiak et al., 2009). Among all structures known to degenerate in HD, the striatum is probably the most affected and its volume has been proposed as a reliable biomarker of HD progression (Hobbs et al., 2010; Paulsen et al., 2008). In this study, we measured the striatum volume of all mice in order to document brain alteration in Ki140CAG mice at 12 month of age. The mean striatal volume of WT littermates, heterozygous and homozygous mice were respectively $18.7 \pm 0.7 \text{ mm}^3$, $16.8 \pm 0.7 \text{ mm}^3$ and $14.8 \pm 0.8 \text{ mm}^3$ (Fig. 2, white, gray and black bars respectively). Homozygous mice exhibited a significant 20.9% decrease of striatal volume compare to WT littermates ($p = 0.002$) whereas the decrease was not significant in heterozygous group in spite of a trend to striatum atrophy (-10.1% , $p = 0.11$).

^1H MRS

Raw spectra acquired with the cryoprobe in the left striatum of one mouse of each group are shown in Fig. 3 (WT mouse: left panel; heterozygous mouse: middle panel; homozygous mouse: right panel). The metabolic profiles acquired in WT littermates, heterozygous and homozygous mice groups are shown in Fig. 4 (white, gray and black

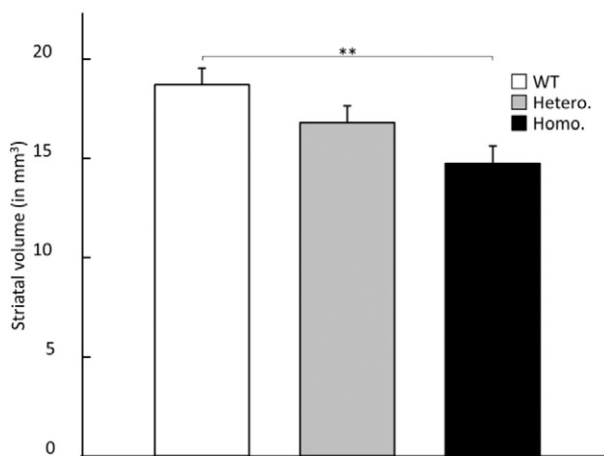


Fig. 2. Striatal atrophy measured by MRI. Striatum volume was measured in WT littermate controls, heterozygous and homozygous mice (white, gray and black bars respectively, mean \pm SEM, $n = 5$ for each group). Statistical analysis was performed by one-way ANOVA (significant threshold set to 0.05) with Fisher's LSD post-hoc test (** $p < 0.01$).

bars respectively). The most striking changes were decreases of Tau and tNAA metabolites in both HD mice groups. Tau exhibited a significant -25.9% decrease ($p = 0.003$) and a significant -33.3% decrease ($p = 0.0002$) in heterozygous and homozygous Ki140CAG mice respectively and tNAA exhibited a significant -17.4% decrease ($p = 0.009$) and a significant -24.3% decrease ($p = 0.0007$) in heterozygous and homozygous Ki140CAG mice respectively. A significant -13.0% decrease ($p = 0.03$) of Glu was also seen in heterozygous Ki140CAG mice. In homozygous mice, Glu concentrations were reduced by -14.9% but this did not reach statistical significance ($p = 0.06$). Finally, we measured a significant 27.4% ($p = 0.01$) increase of Gln and a significant -21.7% ($p = 0.03$) decrease of tCho in homozygous mice. The same trends were observed in heterozygous mice but they did not reach statistical significance.

gluCEST

An example of gluCEST images acquired at three slice positions in each group of mice and corresponding z -spectrum and MTRAsym are shown in Fig. 5. The gluCEST contrast was comparable throughout the three slices (Fig. 5.a). The gluCEST maps from Ki140CAG mice exhibited decreased gluCEST contrast across the whole brain, reflecting a decrease of glutamate concentration. The decrease of gluCEST contrast in heterozygous mice seemed to be smaller than that in homozygous mice (Fig. 5.a). The mean B_0 shift (0.03 ± 0.03 ppm, Fig. 5.b) and ratio $B_1/B_{1,ref}$ (0.99 ± 0.02 , Fig. 5.c) measured into imaging slices showed the rather good homogeneity of B_0 and B_1 fields through the brain. A ROI was drawn manually in the striatum of each mouse and the z -spectrum and Asymmetrical Magnetization Transfer Ratio (MTRAsym) curve were obtained for these mice (Fig. 5.d and e respectively). Z -spectra and MTRAsym confirmed the more intense gluCEST contrast in the WT littermate mouse compare to heterozygous or homozygous mice (Fig. 5.d and e, blue, red and green lines respectively). Mean MTRAsym of WT littermates, heterozygous and homozygous mice groups were calculated in the striatum (Fig. 6.a, blue, red and green lines respectively) and in the corpus callosum (Fig. 6.b, blue, red and green lines respectively). Mean MTRAsym curves calculated for each group of mice confirmed the lower gluCEST contrast in homozygous mice observed on individual images. They also confirmed the intermediate gluCEST contrast level in heterozygous mice. Moreover, one can observe that gluCEST contrast at 3 ppm was approximately 20% higher in striatum (mostly gray matter, GM) than in corpus callosum (white matter, WM). This result is consistent with previous gluCEST studies showing higher gluCEST contrast in GM than in WM due to higher glutamate concentrations in GM (Cai et al., 2012, 2013).

In order to perform regional analysis of gluCEST contrast, several Regions of Interest (ROIs) were manually drawn based on the T_2 -weighted reference image. The following structures were delineated: striatum, corpus callosum, motor cortex, piriform cortex, septal nuclei, somatosensory cortex, hypothalamus and substantia innominata (Fig. 7, top panel). Variations of mean gluCEST contrast (expressed in percentage) measured in each ROI were calculated between control WT littermates vs. heterozygous mice and between control WT littermates vs. homozygous mice and reported on a "variation map of gluCEST contrast" for each group of mice (Fig. 7 bottom left and right maps respectively). These variations and corresponding p -values are also given in Table 1. These maps clearly evidenced the existence of differential reductions of Glu in different regions of the brain. They also underscored a "gene-dose" effect; the decrease of glutamate throughout the brain being milder in heterozygous mice than in homozygous mice. The decrease of gluCEST contrast measured in left and right striatum of homozygous mice was significant (-10.7% ($p = 0.040$) and -12.7% ($p = 0.056$) respectively) whereas it did not reach statistical significance for heterozygous mice. Pronounced decreases of gluCEST contrast were also measured in left and right piriform cortices (-11.0% ($p = 0.078$) and -14.0% ($p = 0.015$) respectively) in homozygous mice whereas

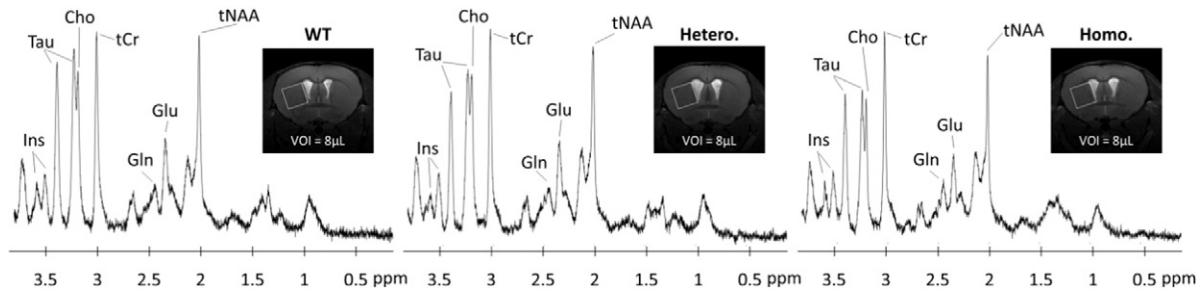


Fig. 3. ^1H MRS of WT littermate and Ki140CAG mice. Examples of ^1H -spectrum acquired in a voxel of $8\ \mu\text{L}$ located in the left striatum of one mouse of each group (WT littermate control mouse: left panel; heterozygous mouse: middle panel; homozygous mouse: right panel). Inset: coronal image centered on mouse striatum with the VOI delimited by the white box. The following metabolites, total choline (*tCho*), total creatine (*tCr*), glutamate (*Glu*), glutamine (*Gln*), myo-inositol (*Ins*), total *N*-acetyl-aspartate + *N*-acetyl-aspartyl-glutamate (*tNAA*) and taurine (*Tau*), were reliably quantified (CRLB <5%).

it did not reach statistical significance for heterozygous mice. Surprisingly, the most affected structure in both heterozygous and homozygous mice was the corpus callosum (-21.8% (p -value = 0.033) and -28.4% (p -value = 0.030) respectively). Interestingly, variations of gluCEST contrasts were consistent between both hemispheres, strongly supporting the idea that measured structure-dependent changes were not related to random inter-regional changes due to an inaccuracy of measurements, but to actual glutamate alterations between brain regions.

Discussion

Behavioral and histological characterization of Ki140CAG mice

In this study, we used a knock-in mouse model of HD which provides a genetically accurate reproduction of the human pathology. This genetic model of HD has already been characterized by slow progression of symptoms as deficits in locomotor performances, behavioral, cellular and molecular abnormalities and neurodegeneration (Menalled et al., 2003).

The behavioral results obtained in the present study showed that both heterozygous and homozygous adult mice exhibited poorer performances than WT littermates. Analysis also showed that homozygous mice seemed to be more affected than heterozygous HD mice in the open-field test. These results suggested that the severity of behavioral signs is stronger in homozygous than in heterozygous

mice, even if difference between heterozygous and homozygous mice did not reach statistical significance because of the small size of mice cohorts. In the rotarod test, both heterozygous and homozygous mice showed poorer performance than WT littermate controls. In this case, homozygous and heterozygous mice appeared similarly affected when comparing the “time to fall” readout. Thus, the notion that homozygous mice are “behaviorally” more affected than heterozygous depends on the test considered. Further characterization and larger animal cohorts are required to fully address this question. However, the qualitative histological evaluation with the EM48 antibody that recognizes huntingtin-positive aggregates showed that homozygous mice had more inclusions than heterozygous mice, supporting the hypothesis that homozygous mice are more affected from a molecular point of view. This is consistent with our recent observations that reduction in the expression of striatal markers (e.g. DARPP-32, *Crym*, *Abdh11os*) is more pronounced in homozygous Ki140CAG mice than in heterozygous (Francelle et al., 2015a,b). The present MRS and MRI data support this view, even though we examined relatively small groups of WT littermates and Ki140CAG mice.

Assessing HD in mice using traditional markers

We measured striatum volume of each mouse using manual segmentation of the brain on anatomical images. These morphometric measures demonstrated atrophy of the striatum in both groups of HD mice. Moreover, the decrease of striatal volume of homozygous mice was two times higher than in heterozygous mice compared to their WT littermates. At 12 months of age, striatal volume appears to be correlated with disease severity, as confirmed by behavioral and histological characterization. This is the first time that a significant atrophy of the striatum is detected by MRI in Ki140CAG mice. This model has been examined by quantitative histological evaluation (stereological cell counts) and no cell loss has been found in the striatum at 12 month of age (Menalled et al., 2003). Our results further support the view that striatal atrophy, even if limited, can occur relatively early. This is consistent with previous studies where striatal volume was shown to be a prodromal marker of HD changes in both HD gene carriers and other animal models and atrophy correlated with severity of symptoms (Myers et al., 1988; Tabrizi et al., 2013). However, even if striatal volume provides interesting clues about structure alterations at macroscopic scale, physiological pathways underlying this striatal alteration remain unknown. For this reason, we searched for more functional alterations, possibly related to defects in energy metabolism and/or neurotransmission using gluCEST imaging.

Metabolic alterations detected by ^1H MRS

From the perspective of identifying relevant and early biological markers of the disease, MRS is promising as it can provide valuable biological information occurring *in vivo* at cellular level (Zacharoff et al.,

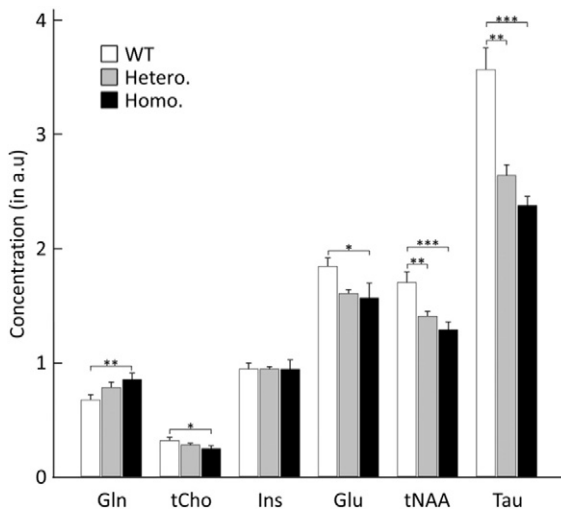


Fig. 4. Metabolic profiles measured by MRS. Concentration of metabolites normalized with respect to 8 mM *tCr* measured in left striatum of WT littermate controls, heterozygous and homozygous mice (white, gray and black bars respectively, mean \pm SEM, $n = 5$ for each group). Statistical analysis was performed by one-way ANOVA (significant threshold set to 0.05) with Fisher’s LSD post-hoc test (*** $p < 0.001$; ** $p < 0.01$; * $p < 0.05$).

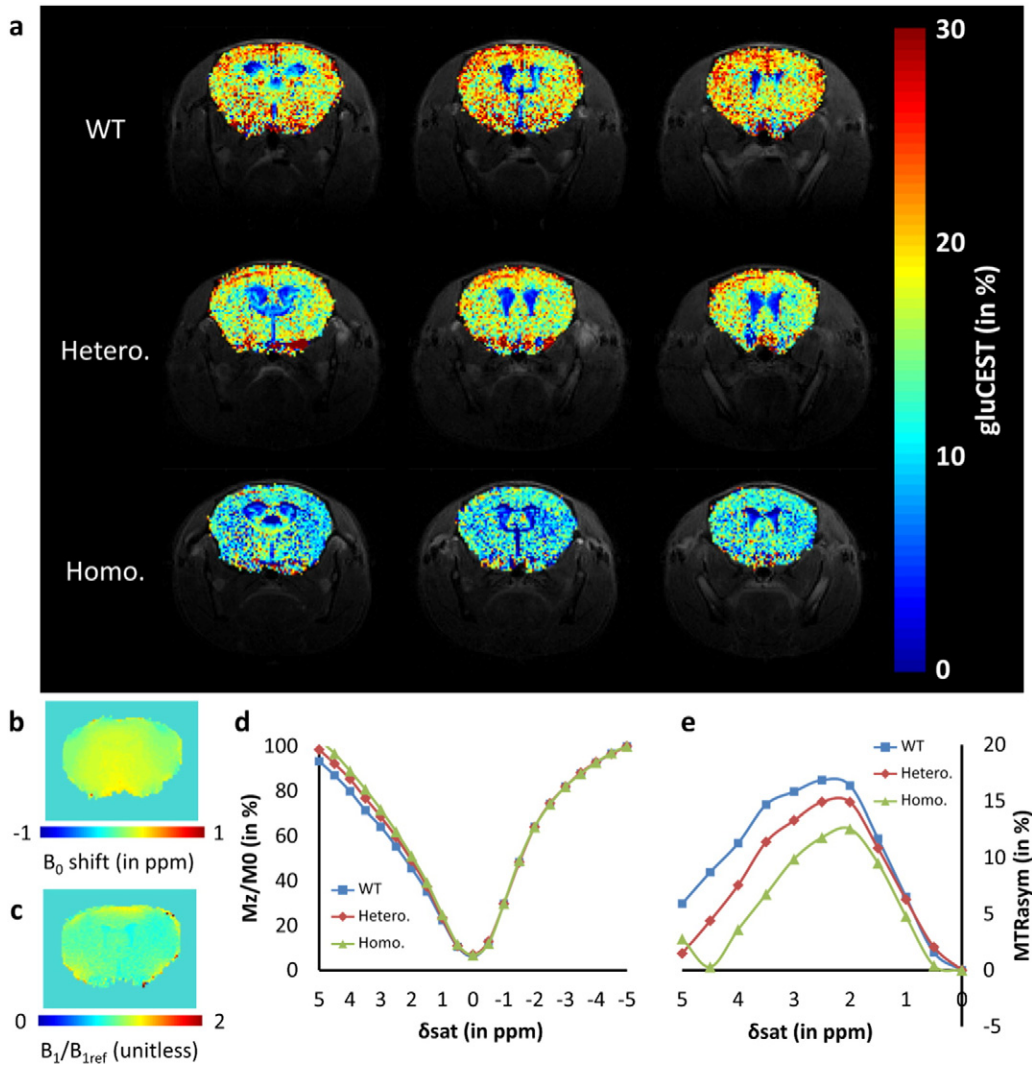


Fig. 5. GluCEST imaging. a) Example of gluCEST images acquired at 3 ppm at three slice positions in each mouse groups (WT littermate control mouse: top panel images; heterozygous mouse: middle panel images; homozygous mouse: bottom panel images). b) Representative B_0 map. c) Representative relative B_1 map. d) Corresponding z-spectra acquired in the striatum of WT littermate, heterozygous and homozygous mice (blue, red and green lines respectively). e) Corresponding MTRasym spectra acquired in the striatum of WT littermate, heterozygous and homozygous mice (blue, red and green lines respectively).

2012). Here, we evidenced that metabolic profiles measured in striatum were significantly different between each group of mice. Notably, we measured a decrease in [Glu], [tNAA] and [Tau] and an increase in [Gln]. The role of Tau in brain metabolism is not well known but several functions have been proposed such as neurotransmission, osmoregulation or neuroprotection (Foos and Wu, 2002; Law, 1998; Tadros et al., 2005). Caution should be taken to interpret the decrease in [Tau] observed in our study but it may reflect a potential alteration of such regulatory processes in the brain of HD mice. Besides, it is usually assumed that Glu and tNAA are essentially located in the neuronal compartment and can be considered as good neuronal markers (Gill et al., 1989; Petroff et al., 1993; Simmons et al., 1991). The decrease of these metabolites suggests alteration of the integrity of neurons and potentially their functions. Indeed, mapping of tNAA distribution using Chemical Shift Imaging (CSI) in the brain of a quinolinic acid rat model revealed regions where tNAA levels recovered, suggesting tNAA as a potential marker of neuronal dysfunction (Shemesh et al., 2010). It has also been shown that decreased tNAA levels may reflect energy production deficit due to mitochondrial impairments (Tabrizi et al., 2000). Indeed, we showed that in non-human primate and rodent models where both the respiratory chain and TCA cycle was partially blocked by the mitochondrial toxin 3-nitropropionic acid, brain NAA

levels assessed by MRS were found decreased in absence of neuronal loss, and returned to control levels when the administration of the neurotoxin was stopped (Dautry et al., 2000).

In our study, the decrease in [Glu] was only significant in heterozygous mice group. In homozygous mice group, one can also observe a clear tendency to [Glu] decrease but the measurement variability and the small size of the cohort prevented from reaching statistical significance ($p = 0.061$). Nonetheless, in spite of non-significant decrease of [Glu] in homozygous mice, the tendency of Glu to decrease argues in favor of its potential involvement in the disease. Modifications in glutamate concentrations could also be indicative of metabolic adaptation and/or defects. Indeed, glutamate is in equilibrium with alpha-ketoglutarate, and is thus directly linked to the Krebs cycle. Krebs cycle defects can lead to brain [Glu] changes, as shown in non-human primates chronically treated with the mitochondrial toxin 3NP (Dautry et al., 1999, 2000). Concomitantly, we measured an increase in [Gln] which is considered to be mainly located in astrocytic cells (Brand et al., 1993). This may reflect a slight inflammation in the brain of HD animals. Such alterations of metabolic profile, with decreased neuronal and increased astrocytic metabolites, are often observed in neurodegenerative diseases. It could suggest an astrocyte/neuron imbalance in energy substrate use and may be indicative of a disturbance

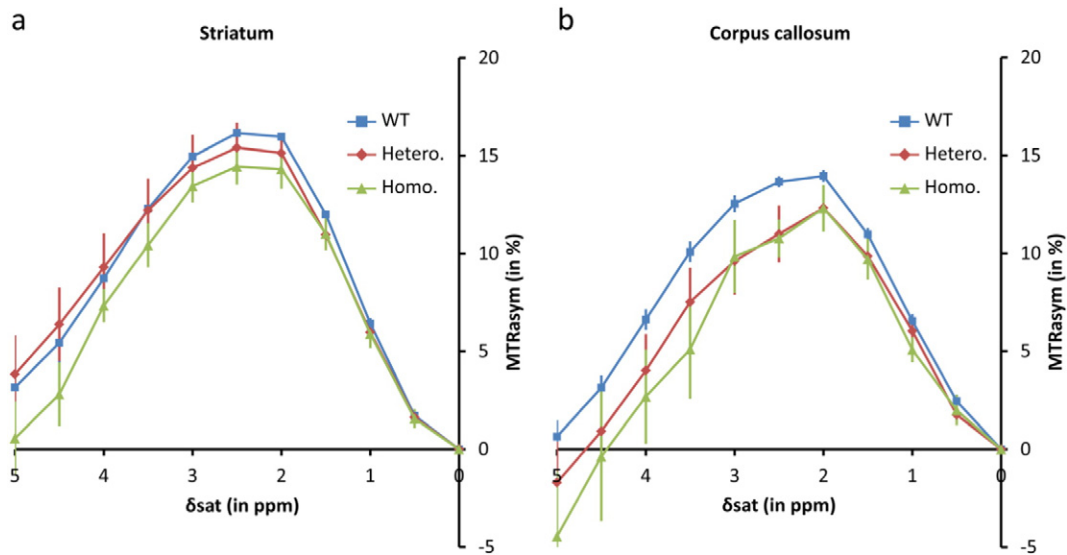


Fig. 6. Comparison of MTRasym measured in striatum and corpus callosum. a) MTRasym spectra acquired in the striatum of WT littermates, heterozygous and homozygous mice (blue, red and green lines respectively). b) MTRasym spectra acquired in the corpus callosum of WT littermates, heterozygous and homozygous mice (blue, red and green lines respectively). Mean values are reported in mean \pm SEM format with $n = 5$ for each group.

of the glutamate/glutamine cycle, which has a central role in energy homeostasis between astrocytes and neurons (Choi et al., 2007).

Previous MRS studies have already been performed on several transgenic mouse models of HD. The transgenic R6/2 mouse is considered as a severe HD model which mimics juvenile onset of HD (Tkac et al., 2012). On the contrary, the knock-in Q111 model is a more

progressive model and reproduces more closely the progression of the disease in HD patients (Menalled et al., 2009). This latter model is closer to our Ki140CAG model which has a late onset of symptom and is slowly progressive. Interestingly, all studies (including ours) showed an increase in Gln and a decrease in tNAA (Jenkins et al., 2000; Tkac et al., 2007), excepted in Q111 where tNAA seemed to remain unchanged

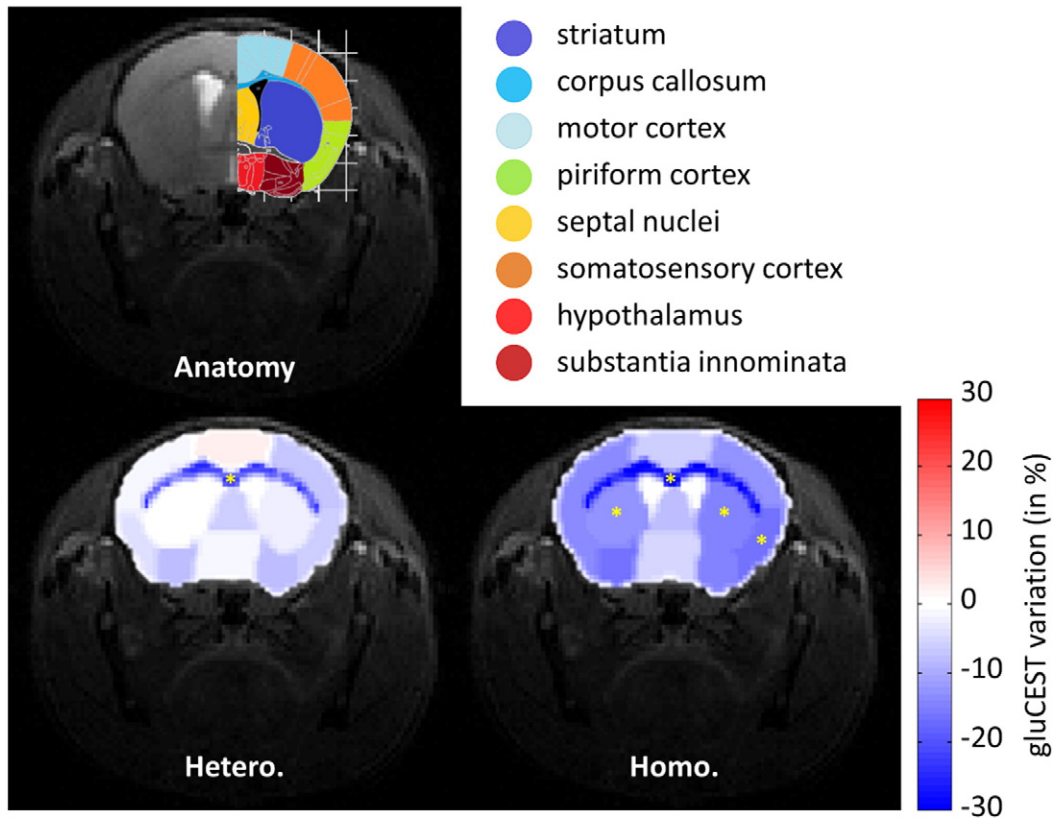


Fig. 7. Variation maps of gluCEST contrasts in Ki140CAG mice. Mice brain was segmented in 8 ROIs (top panel). Variation of gluCEST contrast was calculated in each ROI between WT littermate controls and Ki140CAG mice as follows: Variation = $100 \times (MTRasym(WT) - MTRasym(Ki140CAG)) / MTRasym(WT)$. MTRasym(Ki140CAG) was either mean gluCEST contrast measured in heterozygous mice (bottom left) or in homozygous mice (bottom right). Statistical analysis was performed by one-way ANOVA (significant threshold set to 0.05) with Fisher's LSD post-hoc test (* $p < 0.05$).

Table 1

Variations of gluCEST contrasts. Variations were calculated between WT littermate controls and heterozygous mice (left column), between WT littermate controls and homozygous mice (middle column) and between WT₁ littermate controls and WT₂ littermate controls (right column). Statistical analysis was performed by one-way ANOVA (significant threshold set to 0.05) with Fisher's LSD post-hoc test.

	WT vs. Hetero.		WT vs. Homo.		WT ₁ vs. WT ₂	
	gluCEST variation (in %)	p-Value	gluCEST variation (in %)	p-Value	gluCEST variation (in %)	p-Value
Left striatum	−0.3	0.970	−10.7	0.040	2.0	0.779
Right striatum	−4.3	0.689	−12.7	0.056	2.7	0.592
Corpus callosum	−21.8	0.033	−28.4	0.030	−1.0	0.879
Septal nuclei	−4.8	0.676	−7.0	0.414	−3.6	0.503
Motor cortex	1.6	0.884	−4.7	0.468	1.8	0.845
Left piriform cortex	−3.4	0.721	−11.0	0.078	−2.1	0.665
Right piriform cortex	−5.6	0.572	−14.0	0.015	−1.5	0.725
Left somatosensory cortex	1.5	0.888	−11.1	0.198	0.0	0.996
Right somatosensory cortex	−6.5	0.565	−10.3	0.329	0.3	0.973
Left substantia innominata	−7.5	0.446	−14.2	0.141	−3.6	0.539
Right substantia innominata	−6.7	0.502	−12.0	0.174	0.0	0.997
Hypothalamus	−1.0	0.912	−4.3	0.460	4.0	0.363

(Tkac et al., 2012). The constant tNAA level in Q111 mice can be explained by their relatively young age of scanned mice (13 weeks), whereas symptoms onset appears at 100 weeks or more (Menalled et al., 2009). Consistent decreases in [Glu] and [Tau] were also reported in Q111 mice (Tkac et al., 2012) and in [Glu] in R6/2 mice (Jenkins et al., 2000, 2005).

Glutamate imaging

Changes in brain metabolites observed in HD patients and animal models using MRS provide key insights about disease progression. However, most MRS studies are focused on a specific brain region which is supposed to be early affected in the disease. In the case of HD, a wide majority of studies, including MRS or morphological changes, were performed in the striatum. Nonetheless, recent studies have shown that other brain regions such as the cortex or the corpus callosum were also altered in HD and sometimes earlier than the striatum (Zacharoff et al., 2012). GluCEST imaging offers the possibility to map spatial distribution of Glu in the brain with a good spatial resolution, without a priori knowledge about the structures exhibiting most important metabolic alterations. In this study, gluCEST images were acquired with excellent anatomical resolution, allowing the accurate delineation of several brain regions. While MRS requires rectangular voxel, leading most of the time to partial volume effects, contamination from surrounding structures was limited in gluCEST. The main advantage of gluCEST imaging over MRS is highlighted in the variation maps of glutamate levels calculated between WT littermates and heterozygous mice and between WT littermates and homozygous mice.

To more specifically assess the reproducibility and precision of the gluCEST measurement, we scanned eight additional WT mice, which were randomly divided into two groups (WT₁ and WT₂). The variation map of gluCEST contrasts calculated between WT₁ and WT₂ exhibited small and non-significant variations of gluCEST contrast (Fig. 8). Only small variations of gluCEST contrast can be observed in some brain structures (Table 1, right column) and were most likely due to noise level in gluCEST images. The strongest decrease was measured in the septal nuclei (−3.6% (p -value = 0.503)) whereas the strongest increase was observed in the hypothalamus (+4.0% (p -value = 0.363)), but no gluCEST variation was significant. Hence, one can estimate that a $\pm 4\%$ variation of gluCEST contrast corresponds to the detection threshold of our method under the current experimental conditions. This is much smaller than the significant variations of gluCEST contrast observed in HD mice, strongly reinforcing the validity of our results.

GluCEST contrast measured in HD mice was lower than in their control littermates in almost all brain structures. As gluCEST contrast is almost proportional to glutamate concentration at physiological concentrations (Cai et al., 2012), it is safe to say that glutamate

concentration was decreased in HD mice. Moreover, glutamate loss was more pronounced in homozygous as compared to heterozygous, which is consistent with a faster progression of the disease in this latter group. If striatum exhibited a decrease of glutamate concentration in HD mice, and particularly a significant decrease in homozygous mice (−10.7% (p = 0.040) and −12.7% (p = 0.056) for left and right striatum respectively), obvious variations were also measured in other brain structures. The most striking result was the strong decrease of gluCEST contrast in the corpus callosum observed in both heterozygous and homozygous mice as compared to WT littermates (−21.8% (p = 0.033) and −28.4% (p = 0.030) respectively). Although corpus callosum is not the most studied structure in the context of HD, some previous studies have already demonstrated that this structure could be altered. For instance, decrease of corpus callosum volume was observed in two different mouse models (Lerch et al., 2008; Lerner et al., 2012). Alterations of corpus callosum were also observed in HD patients, notably using diffusion tensor imaging (DTI) (Rosas et al., 2006, 2010; Weaver et al., 2009). These studies have demonstrated that white matter in pre- and early symptomatic HD patients was affected. They demonstrated that changes in diffusion parameters such as fractional anisotropy (FA) and radial diffusivity (RD) were observed in both pre-manifest and HD patients, whereas morphological changes of corpus callosum occurred only in HD patients (Rosas et al., 2010). Moreover, changes in diffusion parameters were detectable several years before changes in corpus callosum thickness, suggesting that alteration

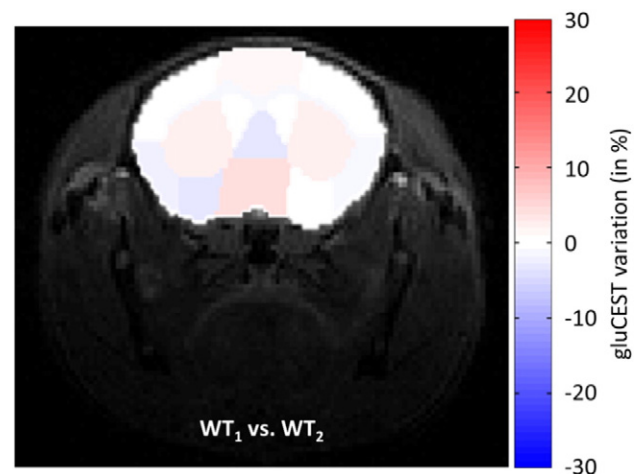


Fig. 8. Variation map of gluCEST contrasts in WT littermate controls. Variation of gluCEST contrasts was measured in 8 ROIs between two groups of WT littermate controls ($n = 4$ in each group).

of structure and functions of afferent axons/myelination occurred before neuronal death. The origin of topographical alteration of corpus callosum was attributed to degeneration of particular cortical regions. Indeed, corpus callosum is mainly composed by fibers connecting left and right hemispheres with axons projecting contra-laterally into the cortex. In the present study, we demonstrated that corpus callosum was the structure exhibiting the largest gluCEST variations in both HD mice groups, indicating that the metabolic pool of glutamate was decreased in those mice. Not expected at first, such alterations of metabolic pool of glutamate could reflect early changes in brain energy metabolism and early compensatory mechanisms to maintain homeostasis, and/or neuronal death. This finding seems consistent with previous studies suggesting a preferential vulnerability of corpus callosum in the context of HD. This may also encourage carrying further studies in order to precisely evaluate its alteration in other neurodegenerative diseases (Teipel et al., 2002; Wiltshire et al., 2005).

We also noticed a decrease of gluCEST contrast in most cortex regions, especially in homozygous mice, but not as significant as in corpus callosum. The larger decrease observed in the corpus callosum might be explained by the fact that corpus callosum is a well-organized and homogeneous structure. So, one can imagine that, if some neurons were altered or suffering, their fraction in a given voxel would be proportionally more important in the corpus callosum compared to a voxel in a structure containing many cell types such as the striatum or the cortex. However, pronounced decreases were observed in homozygous mice in substantia innominata and piriform cortex. The decrease was even more pronounced in this latter structure than in the striatum. Interestingly, several previous studies performed on different mouse models of HD demonstrated that neuronal plasticity was dramatically altered in brain regions involved in olfactory tasks such as piriform cortex (Lazic et al., 2007; van der Borght and Brundin, 2007). Moreover, pioneer work performed on Ki140CAG model demonstrated that htt protein aggregation was also important in the piriform cortex (Menalled et al., 2003), suggesting potential olfactory impairments in those mice. Such deficits in olfaction and especially in odors discrimination were observed in HD patients, even at early stage of the disease (Lazic et al., 2007; Moberg et al., 1987). Our findings seem to corroborate that piriform cortex could be altered in this Ki140CAG mouse model.

In the present study, we explored the potential of CEST imaging to acquire glutamate distribution maps with a good spatial resolution. Similarly to MRS, this is the metabolic pool of glutamate which is probed using gluCEST imaging. However, both techniques are not strictly similar and should be compared with caution. First, comparison between MRS and gluCEST is difficult to perform in strictly identical regions of interest, because signal localization and spatial resolutions are very different in both cases. Furthermore, MRS offers a quantitative “direct” detection of several metabolites whereas gluCEST is able to detect glutamate through magnetization transfer between $-NH_2$ protons and free water protons. Several phenomena, such as magnetic transfer asymmetry or contribution of other exchanging protons from creatine or gamma-aminobutyric acid, may compete with gluCEST contrast and have a minor contribution to the gluCEST contrast (Cai et al., 2012). Such undesirable effects can partially explain small differences between our MRS and gluCEST results and further work will be needed in order to precisely determine potential competing effects in this mouse model. Nonetheless, gluCEST imaging remains a suitable technique to map glutamate alteration levels at high resolution with few contaminations of surrounding structures. Acquisition of a reliable spectrum using MRS in small structures such as the corpus callosum would be much more challenging. Chemical Shift Imaging, which offers an alternative to map metabolic alterations in vivo, has also been proposed to study HD rat models (Beal et al., 1993; Shemesh et al., 2010). However, if the voxel size (a few μL) permitted by CSI was enough to study these models with large excitotoxic lesions in rats, such resolution would have been too large to detect subtle alterations in small brain structures,

especially in mice. Therefore, the partial volume effect in gluCEST imaging is much smaller than in MRS or CSI, giving probably more reliable results in thin structures such as the corpus callosum. Of course, partial volume effects below pixel resolution cannot be excluded, but this is a general problem in imaging. However, since all structures surrounding the corpus callosum appear to be less affected than the corpus callosum itself (including potential partial volume effects), we must conclude that partial volume effects can only result in an underestimation of the gluCEST variation in the corpus callosum. In that context, the conclusions of the paper remain unchanged: the corpus callosum is indeed the most affected structure, but the actual drop of gluCEST effect in pure corpus callosum (far from the edge, excluding all potential partial volume effects) may actually be slightly stronger than reported.

Recent studies have demonstrated the feasibility of gluCEST imaging in healthy human brain and spinal cord (Cai et al., 2012, 2013; Kogan et al., 2013) and also in patients with temporal lobe epilepsy (Davis et al., 2015) at 7 T. In spite of SAR deposition limitations required for safe human imaging and hardware restrictions of clinical scanner, these studies showed the potential of gluCEST imaging to map with a good resolution the actual glutamate distribution in brain and spinal cord. The fast exchange regime of $-NH_2$ protons requires high magnetic fields (≥ 7 T), but the increasing availability of clinical 7 T scanners may open the possibility to evaluate gluCEST imaging to monitor human HD patients.

Conclusion

In this study, we used a knock-in mouse model of Huntington's disease (Ki140CAG) in order to evaluate the interest of gluCEST imaging as a relevant biomarker of HD. We demonstrated that gluCEST contrast was decreased in most of brain regions in homozygous mice as compared to their control littermates. The decrease was smaller in heterozygous mice brain which was consistent with a slower progression of the disease in those mice. Atrophy and MRS-detected metabolic content of the striatum also displayed the same trend. All results indicated modification of metabolism in the brain of HD animal which might be due to metabolic adaptation and/or defects. Interestingly, the good spatial resolution offered by gluCEST imaging allowed identification of region-specific alterations. The corpus callosum seemed to be the most affected brain structure in this mouse model, as largest gluCEST contrast variations were measured in this region in both HD cohorts. This result emphasizes the potential of gluCEST imaging for characterizing metabolic defects in neurodegenerative diseases in specific brain regions. As gluCEST method has already been successfully implemented on high-field clinical scanners (Cai et al., 2013), its evaluation in both pre-manifest and HD patients would be of high interest in order to better understand the physiopathological pathways involving glutamate in HD.

Acknowledgments

We thank Dr. S. Zeitlin, Dr. M. Levine and Dr. Humbert for their help in getting the breeders for starting our Ki140CAG mouse colony. We are grateful J. Mitja for taking care of the animal and helping with behavioral studies. This work was supported by a grant from Agence Nationale pour la Recherche (“HDeNERGY” project, ANR-14-15CE-0007-01). The 11.7 T MRI scanner was funded by a grant from NeurATRIS: A Translational Research Infrastructure for Biotherapies in Neurosciences (“Investissements d’Avenir”, ANR-11-INBS-0011).

References

- Aylward, E.H., Sparks, B.F., Field, K.M., Yallapragada, V., Shpritz, B.D., Rosenblatt, A., Brandt, J., Gourley, L.M., Liang, K., Zhou, H., Margolis, R.L., Ross, C.A., 2004. Onset and rate of striatal atrophy in preclinical Huntington disease. *Neurology* 63, 66–72.
- Beal, M.F., 2005. Mitochondria take center stage in aging and neurodegeneration. *Ann. Neurol.* 58, 495–505.

- Beal, M.F., Brouillet, E., Jenkins, B.G., Ferrante, R.J., Kowall, N.W., Miller, J.M., Storey, E., Srivastava, R., Rosen, B.R., Hyman, B.T., 1993. Neurochemical and histologic characterization of striatal excitotoxic lesions produced by the mitochondrial toxin 3-nitropropionic acid. *J. Neurosci.* 13, 4181–4192.
- Bossy, B., Perkins, G., Bossy-Wetzel, E., 2008. Clearing the brain's cobwebs: the role of autophagy in neuroprotection. *Curr. Neuropharmacol.* 6, 97–101.
- Boussicault, L., Herard, A.S., Calingasan, N., Petit, F., Malgorn, C., Merienne, N., Jan, C., Gaillard, M.C., Lerchundi, R., Barros, L.F., Escartin, C., Delzescaux, T., Mariani, J., Hantraye, P., Flint Beal, M., Brouillet, E., Vega, C., Bonvento, G., 2014. Impaired brain energy metabolism in the BACHD mouse model of Huntington's disease: critical role of astrocyte-neuron interactions. *J. Cereb. Blood Flow Metab.* 34, 1500–1510.
- Brand, A., Richter-Landsberg, C., Leibfritz, D., 1993. Multinuclear NMR studies on the energy metabolism of glial and neuronal cells. *Dev. Neurosci.* 15, 289–298.
- Brouillet, E., Conde, F., Beal, M.F., Hantraye, P., 1999. Replicating Huntington's disease phenotype in experimental animals. *Prog. Neurobiol.* 59, 427–468.
- Cai, K., Haris, M., Singh, A., Kogan, F., Greenberg, J.H., Hariharan, H., Detre, J.A., Reddy, R., 2012. Magnetic resonance imaging of glutamate. *Nat. Med.* 18, 302–306.
- Cai, K., Singh, A., Roalf, D.R., Nanga, R.P., Haris, M., Hariharan, H., Gur, R., Reddy, R., 2013. Mapping glutamate in subcortical brain structures using high-resolution GluCEST MRI. *NMR Biomed.* 26, 1278–1284.
- Carrillo-de Sauvage, M.A., Flament, J., Bramouille, Y., Ben Haim, L., Guillemier, M., Bernard, A., Auregan, G., Houitte, D., Brouillet, E., Bonvento, G., Hantraye, P., Valette, J., Escartin, C., 2015. The neuroprotective agent CNTF decreases neuronal metabolites in the rat striatum: an in vivo multimodal magnetic resonance imaging study. *J. Cereb. Blood Flow Metab.* 35, 917–921.
- Choi, J.K., Dedeoglu, A., Jenkins, B.G., 2007. Application of MRS to mouse models of neurodegenerative illness. *NMR Biomed.* 20, 216–237.
- Cowan, C.M., Raymond, L.A., 2006. Selective neuronal degeneration in Huntington's disease. *Curr. Top. Dev. Biol.* 75, 25–71.
- Damiano, M., Galvan, L., Deglon, N., Brouillet, E., 2010. Mitochondria in Huntington's disease. *Biochim. Biophys. Acta* 1802, 52–61.
- Dautry, C., Conde, F., Brouillet, E., Mittoux, V., Beal, M.F., Bloch, G., Hantraye, P., 1999. Serial ¹H NMR spectroscopy study of metabolic impairment in primates chronically treated with the succinate dehydrogenase inhibitor 3-nitropropionic acid. *Neurobiol. Dis.* 6, 259–268.
- Dautry, C., Vaufrey, F., Brouillet, E., Bizat, N., Henry, P.G., Conde, F., Bloch, G., Hantraye, P., 2000. Early N-acetylaspartate depletion is a marker of neuronal dysfunction in rats and primates chronically treated with the mitochondrial toxin 3-nitropropionic acid. *J. Cereb. Blood Flow Metab.* 20, 789–799.
- Davis, K.A., Nanga, R.P., Das, S., Chen, S.H., Hadar, P.N., Pollard, J.R., Lucas, T.H., Shinohara, R.T., Litt, B., Hariharan, H., Elliott, M.A., Detre, J.A., Reddy, R., 2015. Glutamate imaging (GluCEST) lateralizes epileptic foci in nonlesional temporal lobe epilepsy. *Sci. Transl. Med.* 7, 309ra161.
- Foos, T.M., Wu, J.Y., 2002. The role of taurine in the central nervous system and the modulation of intracellular calcium homeostasis. *Neurochem. Res.* 27, 21–26.
- Francelle, L., Galvan, L., Gaillard, M.C., Guillemier, M., Houitte, D., Bonvento, G., Petit, F., Jan, C., Dufour, N., Hantraye, P., Elalouf, J.M., De Chaldee, M., Deglon, N., Brouillet, E., 2015a. Loss of the thyroid hormone-binding protein Crym renders striatal neurons more vulnerable to mutant huntingtin in Huntington's disease. *Hum. Mol. Genet.* 24, 1563–1573.
- Francelle, L., Galvan, L., Gaillard, M.C., Petit, F., Bernay, B., Guillemier, M., Bonvento, G., Dufour, N., Elalouf, J.M., Hantraye, P., Deglon, N., de Chaldee, M., Brouillet, E., 2015b. Striatal long noncoding RNA *Abhd110s* is neuroprotective against an N-terminal fragment of mutant huntingtin in vivo. *Neurobiol. Aging* 36 (1601), e1607–e1616.
- Gill, S.S., Small, R.K., Thomas, D.G., Patel, P., Porteous, R., Van Bruggen, N., Gadian, D.G., Kauppinen, R.A., Williams, S.R., 1989. Brain metabolites as ¹H NMR markers of neuronal and glial disorders. *NMR Biomed.* 2, 196–200.
- Harper, P.S., 1991. Huntington's Disease.
- Hobbs, N.Z., Barnes, J., Frost, C., Henley, S.M., Wild, E.J., Macdonald, K., Barker, R.A., Scahill, R.I., Fox, N.C., Tabrizi, S.J., 2010. Onset and progression of pathologic atrophy in Huntington disease: a longitudinal MR imaging study. *AJNR Am. J. Neuroradiol.* 31, 1036–1041.
- Jenkins, B.G., Rosas, H.D., Chen, Y.C., Makabe, T., Myers, R., Macdonald, M., Rosen, B.R., Beal, M.F., Koroshetz, W.J., 1998. ¹H NMR spectroscopy studies of Huntington's disease: correlations with CAG repeat numbers. *Neurology* 50, 1357–1365.
- Jenkins, B.G., Klivenyi, P., Kustermann, E., Andreassen, O.A., Ferrante, R.J., Rosen, B.R., Beal, M.F., 2000. Nonlinear decrease over time in N-acetyl aspartate levels in the absence of neuronal loss and increases in glutamine and glucose in transgenic Huntington's disease mice. *J. Neurochem.* 74, 2108–2119.
- Jenkins, B.G., Andreassen, O.A., Dedeoglu, A., Leavitt, B., Hayden, M., Borchelt, D., Ross, C.A., Ferrante, R.J., Beal, M.F., 2005. Effects of CAG repeat length, HTT protein length and protein context on cerebral metabolism measured using magnetic resonance spectroscopy in transgenic mouse models of Huntington's disease. *J. Neurochem.* 95, 553–562.
- Kim, M., Gillen, J., Landman, B., Zhou, J., van Zijl, P., 2009. Water Saturation Shift Referencing (WASSR) for Chemical Exchange Saturation Transfer (CEST) Experiments. *Magn. Reson. Med.* 61, 1441–1450.
- Kogan, F., Singh, A., Debrosse, C., Haris, M., Cai, K., Nanga, R.P., Elliott, M., Hariharan, H., Reddy, R., 2013. Imaging of glutamate in the spinal cord using GluCEST. *NeuroImage* 77, 262–267.
- Kuwert, T., Lange, H.W., Langen, K.J., Herzog, H., Aulich, A., Feinendegen, L.E., 1989. Cerebral glucose consumption measured by PET in patients with and without psychiatric symptoms of Huntington's disease. *Psychiatry Res.* 29, 361–362.
- Kuwert, T., Lange, H.W., Langen, K.J., Herzog, H., Aulich, A., Feinendegen, L.E., 1990. Cortical and subcortical glucose consumption measured by PET in patients with Huntington's disease. *Brain* 113 (Pt 5), 1405–1423.
- Law, R.O., 1998. The role of taurine in the regulation of brain cell volume in chronically hyponatraemic rats. *Neurochem. Int.* 33, 467–472.
- Lazic, S.E., Goodman, A.O., Grote, H.E., Blakemore, C., Morton, A.J., Hannan, A.J., van Dellen, A., Barker, R.A., 2007. Olfactory abnormalities in Huntington's disease: decreased plasticity in the primary olfactory cortex of R6/1 transgenic mice and reduced olfactory discrimination in patients. *Brain Res.* 1151, 219–226.
- Lerch, J.P., Carroll, J.B., Spring, S., Bertram, L.N., Schwab, C., Hayden, M.R., Henkelman, R.M., 2008. Automated deformation analysis in the YAC128 Huntington disease mouse model. *NeuroImage* 39, 32–39.
- Lerner, R.P., Trejo Martinez Ldel, C., Zhu, C., Chesselet, M.F., Hickey, M.A., 2012. Striatal atrophy and dendritic alterations in a knock-in mouse model of Huntington's disease. *Brain Res. Bull.* 87, 571–578.
- Lin, C.H., Tallaksen-Greene, S., Chien, W.M., Cearley, J.A., Jackson, W.S., Crouse, A.B., Ren, S., Li, X.J., Albin, R.L., Detloff, P.J., 2001. Neurological abnormalities in a knock-in mouse model of Huntington's disease. *Hum. Mol. Genet.* 10, 137–144.
- Liu, G., Gilad, A.A., Bulte, J.W., van Zijl, P.C., McMahon, M.T., 2010. High-throughput screening of chemical exchange saturation transfer MR contrast agents. *Contrast Media Mol. Imaging* 5, 162–170.
- Magistretti, P.J., Allaman, I., 2015. A cellular perspective on brain energy metabolism and functional imaging. *Neuron* 86, 883–901.
- Menalled, L.B., 2005. Knock-in mouse models of Huntington's disease. *NeuroRx* 2, 465–470.
- Menalled, L.B., Chesselet, M.F., 2002. Mouse models of Huntington's disease. *Trends Pharmacol. Sci.* 23, 32–39.
- Menalled, L.B., Sison, J.D., Dragatsis, I., Zeitlin, S., Chesselet, M.F., 2003. Time course of early motor and neuropathological anomalies in a knock-in mouse model of Huntington's disease with 140 CAG repeats. *J. Comp. Neurol.* 465, 11–26.
- Menalled, L., El-Khodor, B.F., Patry, M., Suarez-Farinas, M., Orenstein, S.J., Zahasky, B., Leahy, C., Wheeler, V., Yang, X.W., MacDonald, M., Morton, A.J., Bates, G., Leeds, J., Park, L., Howland, D., Signer, E., Tobin, A., Brunner, D., 2009. Systematic behavioral evaluation of Huntington's disease transgenic and knock-in mouse models. *Neurobiol. Dis.* 35, 319–336.
- Moberg, P.J., Pearson, G.D., Speedie, L.J., Lipsey, J.R., Strauss, M.E., Folstein, S.E., 1987. Olfactory recognition: differential impairments in early and late Huntington's and Alzheimer's diseases. *J. Clin. Exp. Neuropsychol.* 9, 650–664.
- Mochel, F., Haller, R.G., 2011. Energy deficit in Huntington disease: why it matters. *J. Clin. Invest.* 121, 493–499.
- Mochel, F., Charles, P., Seguin, F., Barrault, J., Coussieu, C., Perin, L., Le Bouc, Y., Gervais, C., Carcelain, G., Vassault, A., Feingold, J., Rabier, D., Durr, A., 2007. Early energy deficit in Huntington disease: identification of a plasma biomarker traceable during disease progression. *PLoS One* 2, e647.
- Mochel, F., Durant, B., Meng, X., O'Callaghan, J., Yu, H., Brouillet, E., Wheeler, V.C., Humbert, S., Schiffmann, R., Durr, A., 2012. Early alterations of brain cellular energy homeostasis in Huntington disease models. *J. Biol. Chem.* 287, 1361–1370.
- Myers, R.H., Vonsattel, J.P., Stevens, T.J., Cupples, L.A., Richardson, E.P., Martin, J.B., Bird, E.D., 1988. Clinical and neuropathologic assessment of severity in Huntington's disease. *Neurology* 38, 341–347.
- Paulsen, J.S., Langbehn, D.R., Stout, J.C., Aylward, E., Ross, C.A., Nance, M., Guttman, M., Johnson, S., MacDonald, M., Beglinger, L.J., Duff, K., Kayson, E., Biglan, K., Shoulson, I., Oakes, D., Hayden, M., Predict, H.D.L., Coordinators of the Huntington Study, G., 2008. Detection of Huntington's disease decades before diagnosis: the Predict-HD study. *J. Neurol. Neurosurg. Psychiatry* 79, 874–880.
- Petroff, O.A., Pleban, L., Prichard, J.W., 1993. Metabolic assessment of a neuron-enriched fraction of rat cerebrum using high-resolution ¹H and ¹³C NMR spectroscopy. *Magn. Reson. Med.* 30, 559–567.
- Provencher, S.W., 1993. Estimation of metabolite concentrations from localized in vivo proton NMR spectra. *Magn. Reson. Med.* 30, 672–679.
- Rocher, A.B., Gubellini, P., Merienne, N., Boussicault, L., Petit, F., Gipchtein, P., Jan, C., Hantraye, P., Brouillet, E., Bonvento, G., 2016. Synaptic scaling up in medium spiny neurons of aged BACHD mice: a slow-progression model of Huntington's disease. *Neurobiol. Dis.* 86, 131–139.
- Rosas, H.D., Tuch, D.S., Hevelone, N.D., Zaleta, A.K., Vangel, M., Hersch, S.M., Salat, D.H., 2006. Diffusion tensor imaging in presymptomatic and early Huntington's disease: selective white matter pathology and its relationship to clinical measures. *Mov. Disord.* 21, 1317–1325.
- Rosas, H.D., Lee, S.Y., Bender, A.C., Zaleta, A.K., Vangel, M., Yu, P., Fischl, B., Pappu, V., Onorato, C., Cha, J.H., Salat, D.H., Hersch, S.M., 2010. Altered white matter microstructure in the corpus callosum in Huntington's disease: implications for cortical "disconnection". *NeuroImage* 49, 2995–3004.
- Sawiak, S.J., Wood, N.L., Williams, G.B., Morton, A.J., Carpenter, T.A., 2009. Use of magnetic resonance imaging for anatomical phenotyping of the R6/2 mouse model of Huntington's disease. *Neurobiol. Dis.* 33, 12–19.
- Shemesh, N., Sadan, O., Melamed, E., Offen, D., Cohen, Y., 2010. Longitudinal MRI and MRSI characterization of the quinolinic acid rat model for excitotoxicity: peculiar apparent diffusion coefficients and recovery of N-acetyl aspartate levels. *NMR Biomed.* 23, 196–206.
- Simmons, M.L., Frondoza, C.G., Coyle, J.T., 1991. Immunocytochemical localization of N-acetyl-aspartate with monoclonal antibodies. *Neuroscience* 45, 37–45.
- Sonnwald, U., 2014. Glutamate synthesis has to be matched by its degradation — where do all the carbons go? *J. Neurochem.* 131, 399–406.
- Stollberger, R., Wach, P., 1996. Imaging of the active B-1 field in vivo. *Magn. Reson. Med.* 35, 246–251.
- Sturrock, A., Laule, C., Decolongo, J., Dar Santos, R., Coleman, A.J., Creighton, S., Bechtel, N., Reilmann, R., Hayden, M.R., Tabrizi, S.J., Mackay, A.L., Leavitt, B.R., 2010. Magnetic resonance spectroscopy biomarkers in premanifest and early Huntington disease. *Neurology* 75, 1702–1710.

- Sugars, K.L., Rubinsztein, D.C., 2003. Transcriptional abnormalities in Huntington disease. *Trends Genet.* 19, 233–238.
- Sun, P., van Zijl, P., Zhou, J., 2005. Optimization of the irradiation power in chemical exchange dependent saturation transfer experiments. *J. Magn. Reson.* 175, 193–200.
- Tabrizi, S.J., Workman, J., Hart, P.E., Mangiarini, L., Mahal, A., Bates, G., Cooper, J.M., Schapira, A.H., 2000. Mitochondrial dysfunction and free radical damage in the Huntington R6/2 transgenic mouse. *Ann. Neurol.* 47, 80–86.
- Tabrizi, S.J., Scahill, R.I., Owen, G., Durr, A., Leavitt, B.R., Roos, R.A., Borowsky, B., Landwehrmeyer, B., Frost, C., Johnson, H., Craufurd, D., Reilmann, R., Stout, J.C., Langbehn, D.R., Investigators, T.-H., 2013. Predictors of phenotypic progression and disease onset in premanifest and early-stage Huntington's disease in the TRACK-HD study: analysis of 36-month observational data. *Lancet Neurol.* 12, 637–649.
- Tadros, M.G., Khalifa, A.E., Abdel-Naim, A.B., Arafa, H.M., 2005. Neuroprotective effect of taurine in 3-nitropropionic acid-induced experimental animal model of Huntington's disease phenotype. *Pharmacol. Biochem. Behav.* 82, 574–582.
- Teipel, S.J., Bayer, W., Alexander, G.E., Zebuhr, Y., Teichberg, D., Kulic, L., Schapiro, M.B., Moller, H.J., Rapoport, S.I., Hampel, H., 2002. Progression of corpus callosum atrophy in Alzheimer disease. *Arch. Neurol.* 59, 243–248.
- Tkac, I., Dubinsky, J.M., Keene, C.D., Gruetter, R., Low, W.C., 2007. Neurochemical changes in Huntington R6/2 mouse striatum detected by in vivo ^1H NMR spectroscopy. *J. Neurochem.* 100, 1397–1406.
- Tkac, I., Henry, P.G., Zacharoff, L., Wedel, M., Gong, W., Deelchand, D.K., Li, T., Dubinsky, J.M., 2012. Homeostatic adaptations in brain energy metabolism in mouse models of Huntington disease. *J. Cereb. Blood Flow Metab.*
- van der Borght, K., Brundin, P., 2007. Reduced expression of PSA-NCAM in the hippocampus and piriform cortex of the R6/1 and R6/2 mouse models of Huntington's disease. *Exp. Neurol.* 204, 473–478.
- van Zijl, P.C., Yadav, N.N., 2011. Chemical exchange saturation transfer (CEST): what is in a name and what isn't? *Magn. Reson. Med.* 65, 927–948.
- Walker, F.O., 2007. Huntington's disease. *Lancet* 369, 218–228.
- Ward, K.M., Balaban, R.S., 2000. Determination of pH using water protons and chemical exchange dependent saturation transfer (CEST). *Magn. Reson. Med.* 44, 799–802.
- Ward, K.M., Aletras, A.H., Balaban, R.S., 2000. A new class of contrast agents for MRI based on proton chemical exchange dependent saturation transfer (CEST). *J. Magn. Reson.* 143, 79–87.
- Weaver, K.E., Richards, T.L., Liang, O., Laurino, M.Y., Samii, A., Aylward, E.H., 2009. Longitudinal diffusion tensor imaging in Huntington's disease. *Exp. Neurol.* 216, 525–529.
- Wheeler, V.C., White, J.K., Gutekunst, C.A., Vrbanc, V., Weaver, M., Li, X.J., Li, S.H., Yi, H., Vonsattel, J.P., Gusella, J.F., Hersch, S., Auerbach, W., Joyner, A.L., MacDonald, M.E., 2000. Long glutamine tracts cause nuclear localization of a novel form of huntingtin in medium spiny striatal neurons in HdhQ92 and HdhQ111 knock-in mice. *Hum. Mol. Genet.* 9, 503–513.
- Wheeler, V.C., Gutekunst, C.A., Vrbanc, V., Lebel, L.A., Schilling, G., Hersch, S., Friedlander, R.M., Gusella, J.F., Vonsattel, J.P., Borchelt, D.R., MacDonald, M.E., 2002. Early phenotypes that presage late-onset neurodegenerative disease allow testing of modifiers in Hdh CAG knock-in mice. *Hum. Mol. Genet.* 11, 633–640.
- Wiltshire, K., Foster, S., Kaye, J.A., Small, B.J., Camicioli, R., 2005. Corpus callosum in neurodegenerative diseases: findings in Parkinson's disease. *Dement. Geriatr. Cogn. Disord.* 20, 345–351.
- Wolff, S., Balaban, R., 1990. NMR imaging of labile proton exchange. *J. Magn. Reson.* 86, 164–169.
- Zacharoff, L., Tkac, I., Song, Q., Tang, C., Bolan, P.J., Mangia, S., Henry, P.G., Li, T., Dubinsky, J.M., 2012. Cortical metabolites as biomarkers in the R6/2 model of Huntington's disease. *J. Cereb. Blood Flow Metab.* 32, 502–514.
- Zhou, J., van Zijl, P.C.M., 2006. Chemical exchange saturation transfer imaging and spectroscopy. *Prog. Nucl. Magn. Reson. Spectrosc.* 48.